International Journal of Heat and Mass Transfer 52 (2009) 4400–4412

Contents lists available at ScienceDirect

International Journal of Heat and Mass Transfer

journal homepage: www.elsevier.com/locate/ijhmt

Direct and inverse mixed convections in an enclosure with ventilation ports

Fu-Yun Zhao [a,*], Di Liu [b], Li Tang [c], Yu-Long Ding [a], Guang-Fa Tang [b]

[a] School of Process, Environmental and Materials Engineering, University of Leeds, Leeds LS2 9JT, UK
[b] College of Civil Engineering, Hunan University, Changsha, Hunan 410082, PR China
[c] School of Civil and Architecture Engineering, Central South University, Changsha, Hunan 410075, PR China

ARTICLE INFO

Article history:
Received 17 February 2009
Accepted 19 March 2009
Available online 4 May 2009

Keywords:
Enclosure flows
Direct mixed convection
Inverse mixed convection
Heatlines

ABSTRACT

The numerical study presented in this work describes the direct and inverse mixed convection problems in a slot-ventilated enclosure subjected to an unknown heat flux on one side. Particularly, the interaction of internal natural convection with the cold ventilated flow leads to various flow fields depending on the Richardson number, Reynolds number, and the functional form of the imposed boundary heat flux. Fluid and heat transport structures across the enclosure are visualized by the streamlines and heatlines, respectively. Subsequently, an iterative conjugate gradient method is applied such that the gradient of the cost function is introduced when the appropriate sensitivity and adjoint problems are defined for a domain of arbitrary geometries. In this approach, no a priori information is needed about the unknown boundary heat fluxes to be determined. The accuracy of the heat flux profile solutions is shown to depend strongly on the values of Reynolds number and flux functional forms. Effects of measurement errors on the accuracy of estimation are also investigated. The present work is significant for the flow control simultaneously involving the natural convection and forced convection.

1. Introduction

Combined forced and natural convection is often encountered in electronic cooling, room ventilation, fluid flows in chemical reactors, cooling of large power plants, to name just a few [1,2]. The interaction between a buoyancy-induced thermal plume from heat sources and an externally driven cold flow inside a cavity constitutes a typical configuration, where the behavior of mixed convection has been investigated for different values of Reynolds number, Richardson number, fluid properties, positions of heat source and ventilation port, and geometries [3–20]. Three different regimes were observed, namely, natural convection, comparable natural and forced convection, and forced convection. Concomitantly, transitional, oscillatory or multiple flows caused by the interaction between forced and free convection have also been investigated [6–10,12,14,15,18,19].

As expected, the aforementioned mixed convection in enclosures could be well defined once the thermal conductivity, velocity and temperature or heat fluxes are specified on the whole boundary of the domain. This is called the direct mixed convection problem [1,2,19,21]. Inversely, the fluid flow and heat transfer within a domain are not well defined if the velocity, temperature and heat flux are not specified along some surface or arbitrary locations lying inside the domain. This is called the inverse problem, which is of great importance from many practical points of view (analysis, control and design) and has aroused an increasing interest during the last few decades. Literature review shows that the existing plentiful studies were, however, limited to the inverse heat conduction problem [22,23,42]. Comparing with the studies of inverse conduction problem, inverse convection problem is more difficult to investigate as the flow field is dynamically coupled with the heat convection [24–29]. This is due to the fact that fluid flow introduces new physics such as boundary layers and vortex formation, which in turn localizes the region where sensitive information is contained.

In the present work, we examine the inverse heat transfer problem in an enclosure simultaneously involving natural convection and forced convection, which is still unexplored. Contrary to the mixed convection problem which consists of computing the consequences of given causes, the inverse mixed convection problem is associated with the reversal of the cause-effect sequence and consists of finding the unknown causes of known consequences. The effects of mixed convection on the stability and accuracy of the inverse solution should be analyzed in terms of thermal Grashof number, Reynolds number, number and position of sensors.

The next section presents the physical model of mixed convection in an enclosure ventilated by two ports. Subsequently, detailed derivation of the sets of sensitivity and adjoint equations used in the Conjugate Gradient Method [24–29] would

* Corresponding author. Tel.: +44 (0) 113 343 2543; fax: +44 (0) 113 343 2406.
E-mail addresses: F.Y.Zhao@leeds.ac.uk, zfycfdnet@163.com (F.-Y. Zhao), liudi66@163.com (D. Liu).

0017-9310/$ - see front matter © 2009 Elsevier Ltd. All rights reserved.
doi:10.1016/j.ijheatmasstransfer.2009.03.017

Nomenclature

E	cost functional/performance function
FED	accuracy of estimation
g	gravitational acceleration
Gr	Grashof number
K	CGM iteration loop
L	size of the square enclosure
M	number of sensors
P	dimensionless pressure
Pr	Prandtl number
ps	conjugate search direction
Q	dimensionless heat flux
Re	Reynolds number
Ri	Richardson number
T	dimensionless temperature
U, V	dimensionless velocity components
X, Y	dimensionless Cartesian coordinates

Greeks

α	step size for CGM
ε	small number
$\delta T, \delta \mathbf{U}$	sensitivity variables
σ	dimensionless standard deviation
τ	dimensionless time
Γ	piecewise boundary
π, ξ, η	adjoint variables
Ψ	stream function
Θ	heat function
Ω	domain

Subscripts

in, out	inlet and outlet
kq, uq	known and unknown heat fluxes
kt, ut	known and unknown temperatures
m	measurement
k	known
u	unknown

Superscript

*	dimensional variable

be presented concerning the combined forced and natural convection. Numerical results, including fluid and heat transport structures [19,30–35], will be presented next to show the effects of convection flow, boundary conditions and noisy data on the convergence and accuracy of the inverse solutions.

2. Combined forced and natural convection

Fig. 1(a) presents a general sketch of the enclosed domain Ω with piecewise smooth and non-overlapped boundaries Γ_{kq}, Γ_{uq}, Γ_{kt}, Γ_{in}, and Γ_{out}, satisfied with $\Gamma_{kq} \cup \Gamma_{uq} \cup \Gamma_{kt} = \Gamma$. The domain is of an arbitrary geometry, and the Cartesian coordinates (x, y) with the corresponding velocity components (u, v), are indicated herein. It is assumed that the dimension in the z direction is large enough and the end effects on the flow are negligible, i.e., fluid flow and heat transfer is two-dimensional. The fluid is initially at rest and the uniform temperature t_0. At $\tau^* = 0$, the boundaries Γ_{kq}, Γ_{uq}, Γ_{kt}, Γ_{in}, and Γ_{out} are, respectively, subjected to the space-dependent heat fluxes Q_k^*, Q_u^*, temperature t_k, inflow $(\boldsymbol{u}_{in}, t_{in})$ and outflow $(\boldsymbol{u}_{out}, t_{out})$, and the mixed convective flow is then initiated and evolves. Non-slip boundary conditions are imposed over the inner surfaces Γ of the domain. It should also be pointed out that radiation effects were not included in this study, since this would overly complicate the problem. In practical terms, the results obtained here would apply to surfaces of sufficiently low emissivity, so that the radiation effects relative to those of buoyancy and forced convection can be neglected.

The fluid flow and heat transfer are governed by the continuity, Navier–Stokes and energy equations. The effect of thermal buoyancy due to the heat input is taken into account for the fluid flow inside the enclosure. The Boussinesq approximations are applied for the density variations. The compressibility work and the viscous dissipation terms are neglected in the energy equation. With the foregoing assumptions, the equations for the two-dimensional flow under consideration are written in the conservative non-dimensional form, respectively, as

$$\nabla \cdot \mathbf{U} = 0 \tag{1}$$

$$\frac{\partial \mathbf{U}}{\partial \tau} + \mathbf{U} \cdot (\nabla \mathbf{U}) = \nabla \cdot \left[-\mathbf{P} + \frac{1}{Re} \nabla \mathbf{U} \right] - \frac{Gr}{Re^2} T \cdot \mathbf{e}_g \tag{2}$$

$$\frac{\partial T}{\partial \tau} + \mathbf{U} \cdot (\nabla T) = \frac{1}{Re\,Pr} \nabla^2 T \tag{3}$$

The aforementioned non-dimensional equations were obtained through introducing the following relations:

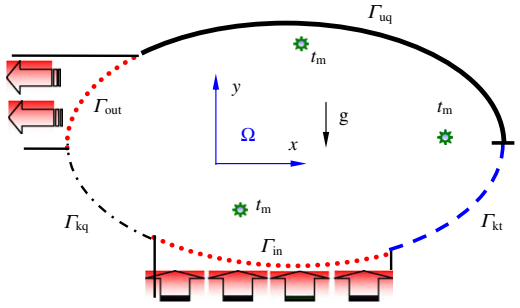

(a) General geometry of mixed convection and inverse mixed convection

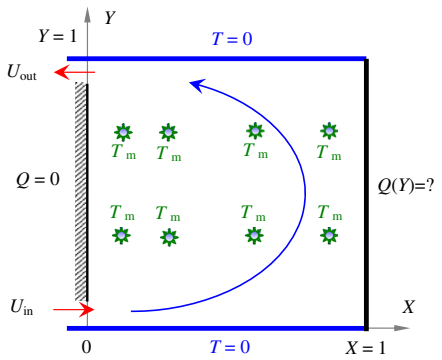

(b) Schematic of the square cavity, the coordinate system and boundary conditions

Fig. 1. The geometry of the flow configuration under consideration along with the coordinate system.

$$(X,Y)=(x,y)/L,\quad (U,V)=(u,v)/u_0,\quad \tau=\tau^*/(L/u_0) \tag{4a}$$

$$P=(p+\rho_0 gy)/[\rho(u_0)^2],\quad T=(t-t_0)/\Delta t,\quad Q=Q^*/q_0 \tag{4b}$$

Correspondingly, the governing parameters are defined as

$$Pr=v/\alpha_F,\quad Gr=g\beta\Delta tL^3/v^2,\quad Re=u_0L/v \tag{5}$$

where, the temperature potential Δt is given by q_0L/k. The symbols ρ, g, v, α_F, and β denote, respectively, the density, gravitational acceleration, kinematic viscosity, thermal diffusivity, and coefficient of volumetric expansion. It may be noted here that in defining the Reynolds number, *Re*, the length scale chosen is size of the enclosure *L* (as shown in Fig. 1(b)). This allows the width of the inlet (outlet) to appear in the boundary conditions. The relative magnitude of the Grashof number *Gr* and Reynolds number *Re*, the Richardson number $Ri = Gr/Re^2$, determines which one of the two mechanisms of flow is predominant.

As shown in Fig. 1(a), the corresponding boundary conditions are written as

$$(U,V)=0,\quad (X,Y)\epsilon\Gamma_{kq}\upsilon\Gamma_{uq}\upsilon\Gamma_{kt} \tag{6}$$

$$T=T_k(X,Y),\quad (X,Y)\epsilon\Gamma_{kt} \tag{7}$$

$$-\nabla T\cdot n=Q_k(X,Y),\quad (X,Y)\epsilon\Gamma_{kq} \tag{8}$$

$$-\nabla T\cdot n=Q_u(X,Y),\quad (X,Y)\epsilon\Gamma_{uq} \tag{9}$$

$$\mathbf{U}=\mathbf{U}_{in}(X,Y),\quad T=T_{in}(X,Y),\quad (X,Y)\epsilon\Gamma_{in} \tag{10}$$

The sensitivity of the solution to the outflow boundary conditions should be tested through the comparison of Dirichlet and Neumann boundary conditions; typically, the zero gradient condition is compared against specifying the same flow conditions at the outflow as at the inflow. Slight discrepancies are felt only in the flow field near the outflow boundary, while the effect on the flow and heat transfer results over the rest of the computational domain are insignificant. As a result, the following outflow boundary conditions are considered in the present work:

$$P+\nabla\tau_n\cdot n=0,\quad -\nabla T\cdot n=0,\quad (X,Y)\epsilon\Gamma_{out} \tag{11}$$

where τ_n represents the stress tensor normal to the Γ_{out}. If the unknown boundary condition Q_u were known a priori, the fluid and thermal flow across the system Ω can be obtained through solving the aforementioned equations, i.e., direct mixed convection problem [1,2,19]. Additionally, the following initial conditions are also employed:

$$\mathbf{U}(X,Y,\tau=0)=0,\quad \text{and}\quad T(X,Y,\tau=0)=0,\quad (X,Y)\epsilon\Omega \tag{12}$$

The streamlines and heatlines are the best choice to visualize the paths followed by the fluid and heat flows [19,30–35]. Such lines are defined, respectively, as the constant lines of the streamfunction (Ψ) and heatfunction (Θ). The dimensionless forms can be obtained

$$\frac{\partial\Psi}{\partial Y}=U,\quad -\frac{\partial\Psi}{\partial X}=V \tag{13}$$

$$\frac{\partial\Theta}{\partial Y}=RePrUT-\frac{\partial T}{\partial X},\quad -\frac{\partial\Theta}{\partial X}=RePrVT-\frac{\partial T}{\partial Y} \tag{14}$$

The Ψ and Θ fields are defined through its first order derivatives, being thus important only differences in its values but not its level. This relative nature is similar to that of the pressure field in incompressible fluid flows. Thus, we have the freedom to state that

$$\Psi(0,0)=\Theta(0,0)=0 \tag{15}$$

As a heat transfer visualization technique, the use of heatlines is the convection counterpart or the generalization of a standard technique (heat-flux lines) used in heat conduction. If the fluid flow subsides ($U = V = 0$), the heatlines become identical to the heat-flux lines employed frequently in the study of conduction phenomena [31].

3. Inverse mixed convection problem

The aforementioned mixed convection problem associated with the mathematical formulation given by Eqs. (1)–(12), involves the determination of the velocity and temperature fields in the enclosure, from the knowledge of the enclosure geometry, of the physical properties and of the initial and boundary conditions. Appropriately formulated direct mixed convection problems are mathematically classified as well-posed. The solution of a well-posed problem must satisfy the conditions of existence, uniqueness and stability with respect to the input data.

For the inverse mixed convection problem, we should determine the boundary heat flux Q_u with the known boundary conditions and the measured or designed temperatures due to the fact that temperature field inside the domain can be easily measured at various locations. Differing from direct problems, inverse problems are mathematically classified as ill-posed due to the fact that the solution may not exist or may not be unique or stable. Actually, a successful solution of an inverse convection problem generally involves its reformulation as an approximate well-posed problem and makes use of some kind of regularization (stabilization) technique. In the present work, a solution to the inverse mixed convection problem would be assumed existed in the sense of Tichonov [22,23]. Particularly, we look for the boundary heat flux Q_u that will minimize the following error:

$$E(Q_u)=\frac{1}{2}\int_0^{\tau_f}\sum_{i=1}^{M}[T(X_i,Y_i,\tau)-T_m(X_i,Y_i,\tau)]^2d\tau \tag{16}$$

where, T and T_m are the numerical-predicted and on-site-measured temperatures at the sensor's position, respectively. M is the total number of sensors. Although only steady flow situation is considered in the present work, the time integration over the measurement points makes the formula more general.

Admittedly, if Q_u is a function of time only, not more than one single sensor is needed to get a valid solution. For a non-uniform heat flux of arbitrary form, a continuum set of sensors is required in principle. Simultaneously, one should observe that the inverse mixed convection problem in which the calculation of Q_u is achieved using known temperature measurements within the domain or at some boundary locations. The number of sensors, their location and accuracy become crucial to the solution of the inverse convection problem [28]. However, in the present work, attentions are particularly paid on the effect of mixed convection on the inverse estimations. Thus, the measurement locations and sensors have been maintained constant if there were no other special illustrations.

The sequence of approximations for the unknown heat flux Q_u may be constructed following the steps of the conjugate gradient method [24–27,29], according to $Q_u^{K+1}=Q_u^K+\alpha^K ps^K$, where α is the step size and *ps* the conjugate search direction. The search direction *ps* is related to the gradient of the cost functional E with respect to Q_u, whose function shape is not available for general cases. The gradient of the cost functional E and the step size α must be obtained, respectively, from the solution of the adjoint and sensitivity problems described below.

3.1. Sensitivity problem

The main difficulty of the foregoing inverse problem is the calculation of the gradient of the cost functional in the Γ_{uq} space. Let us introduce the temperature sensitivity δT as the directional derivative of T at Q_u in the direction δQ_u, which is equal to

$$\delta T=\lim_{\varepsilon\to 0}\frac{T(Q_u+\varepsilon\delta Q_u)-T(Q_u)}{\varepsilon} \tag{17}$$

where ε is a small real number. The remaining variables can be done similar to Eq. (17). Based on the definition of the sensitivity variables, it is straightforward to derive the following sets of sensitivity equations, respectively, for continuity, momentum and temperature sensitivities:

$$\nabla\cdot\delta\mathbf{U}=0 \tag{18}$$

$$\frac{\partial\delta\mathbf{U}}{\partial\tau}+\mathbf{U}\cdot(\nabla\delta\mathbf{U})=\nabla\cdot\left[-\delta\mathbf{P}+\frac{1}{Re}(\nabla\delta\mathbf{U})\right]-\delta\mathbf{U}\cdot(\nabla\mathbf{U})-\frac{Gr}{Re^2}\delta T\cdot\mathbf{e}_g \tag{19}$$

$$\frac{\partial\delta T}{\partial\tau}+\mathbf{U}\cdot(\nabla\delta T)=\frac{1}{RePr}\nabla^2\delta T-\delta\mathbf{U}\cdot(\nabla T) \tag{20}$$

Additionally, the sensitivity variables satisfy the same initial and boundary conditions as their direct problem counterparts. As a consequence, the relevant boundary and initial conditions for the set of sensitivity equations can be expressed as follows:

$$(\delta U,\delta V)=0,\quad (X,Y)\epsilon\Gamma_{kq}\upsilon\Gamma_{uq}\upsilon\Gamma_{kt}\upsilon\Gamma_{in} \tag{21}$$

$$\delta P=0,\quad (X,Y)\epsilon\Gamma_{out} \tag{22}$$

$$\delta T=0,\quad (X,Y)\epsilon\Gamma_{kt}\upsilon\Gamma_{in} \tag{23}$$

$$-\nabla\delta T\cdot n=0,\quad (X,Y)\epsilon\Gamma_{kq}\upsilon\Gamma_{out} \tag{24}$$

$$-\nabla\delta T\cdot n=\delta Q_u(X,Y),\quad (X,Y)\epsilon\Gamma_{uq} \tag{25}$$

$$\overrightarrow{\delta U}(X,Y,\tau=0)=0\quad\text{and}\quad \delta T(X,Y,\tau=0)=0,\ (X,Y)\epsilon\Omega \tag{26}$$

These formulations illuminate that the driving force of the sensitivity problem is the heat flux increment δQ_u imposed at the boundary Γ_{uq}.

3.2. Adjoint problem

The calculation of the gradient of the objective function requires the appropriate evaluation of the adjoint operators to the sensitivity operators defined above. In an infinite-dimensional space, the gradient of E must verify the formal equality

$$D_{\delta Q_u}E(Q_u)=\langle\nabla E|\delta Q_u\rangle \tag{27}$$

where the left-hand side is the directional derivative of E at Q_u in the direction δQ_u. The gradient of E may then be determined by a set of adjoint equations as follows. Starting from Eq. (16), the directional derivative of E is

$$D_{\delta Q_u}E(Q_u)=\int_0^{\tau_f}\sum_{i=1}^{M}[T(X_i,Y_i,\tau)-T_m(X_i,Y_i,\tau)]\cdot\delta T(X_i,Y_i,\tau)d\tau \tag{28}$$

where all quantities are evaluated at the sensors' positions (X_m, Y_m). It should be noted that the expression on the right-hand side of Eq. (28) might be expressed using Dirac delta function as an integral over surface and time [24,28]. Introducing the adjoint temperature η, velocity ξ, and pressure π, it is possible to substitute Eqs. (18)–(20) into Eq. (28) such that the directional derivative of E becomes

$$\begin{aligned}D_{\delta Q_u}E(Q_u)=&\int_0^{\tau_f}\int_\Omega(T-T_m)\cdot\delta T\sum_{i=1}^{M}\delta(\vec{r}-\vec{r}_i)d\Omega d\tau\\&+\int_0^{\tau_f}\int_\Omega\vec{\xi}\left[\frac{\partial\overrightarrow{\delta U}}{\partial\tau}+\vec{U}\cdot(\nabla\overrightarrow{\delta U})+\overrightarrow{\delta U}\cdot(\nabla\vec{U})\right.\\&\left.+\nabla\delta P\vec{I}-\frac{1}{Re}\nabla^2\overrightarrow{\delta U}+\frac{Gr}{Re^2}\delta T\cdot\vec{e}_g\right]d\Omega d\tau\\&+\int_0^{\tau_f}\int_\Omega\pi\left[\nabla\cdot\overrightarrow{\delta U}\right]d\Omega d\tau+\int_0^{\tau_f}\int_\Omega\eta\left[\frac{\partial\delta T}{\partial\tau}+\vec{U}\cdot(\nabla\delta T)\right.\\&\left.+\overrightarrow{\delta U}\cdot(\nabla T)-\frac{1}{RePr}\nabla^2\delta T\right]d\Omega d\tau\end{aligned} \tag{29}$$

By employing integration in the last three terms appearing on the right-hand side of Eq. (29), utilizing the initial and boundary conditions of the sensitivity problem for δT, and also requiring that the coefficients of δT in the resulting equation vanish, the following adjoint problems is then obtained:

$$\nabla\cdot\xi=0 \tag{30}$$

$$\frac{\partial\xi}{\partial\tau}+\mathbf{U}\cdot(\nabla\xi)=\nabla\cdot\left[\pi-\frac{1}{Re}(\nabla\xi)\right]+\xi\cdot(\nabla\mathbf{U})^T+\eta\cdot\nabla T \tag{31}$$

$$\frac{\partial\eta}{\partial\tau}+\mathbf{U}\cdot(\nabla\eta)=-\frac{1}{RePr}\nabla^2\eta+\frac{Gr}{Re^2}\xi\cdot\mathbf{e}_g-(T-T_m)\sum_{i=1}^{M}\delta(\mathbf{r}-\mathbf{r}_i) \tag{32}$$

The corresponding initial and boundary conditions are described as

$$(\xi_X,\xi_Y)=0,\quad (X,Y)\epsilon\Gamma_{kq}\upsilon\Gamma_{uq}\upsilon\Gamma_{kt}\upsilon\Gamma_{in} \tag{33}$$

$$\pi=0,\quad (X,Y)\epsilon\Gamma_{out} \tag{34}$$

$$\eta=0,\quad (X,Y)\epsilon\gamma_{kt}\upsilon\Gamma_{in} \tag{35}$$

$$-\nabla\eta\cdot n=0,\quad (X,Y)\epsilon\gamma_{kq}\upsilon\gamma_{uq}\upsilon\Gamma_{out} \tag{36}$$

$$\vec{\xi}(X,Y,\tau=\tau_f)=0,\quad \eta(X,Y,\tau=\tau_f)=0,\quad (X,Y)\epsilon\Omega \tag{37}$$

The set of equations (30)–(32) defines the adjoint problem, together with the conditions imposed on the adjoint variables on the boundary of Ω excluding the section Γ_{uq} and at time τ_f. It should be mentioned that the transformation of temporal variable $\tau' = \tau_f - \tau$ has to be conducted at first, in order to solve the adjoint equation with the "end condition" at the physical time τ_f.

$$\begin{aligned}\frac{\partial\vec{\xi}}{\partial\tau'}-\vec{U}\cdot(\nabla\vec{\xi})=&\nabla\cdot\left[-\pi\vec{I}+\frac{1}{Re}(\nabla\vec{\xi})\right]\\&-\vec{\xi}\cdot(\nabla\vec{U})^T-\eta\cdot\nabla T\end{aligned} \tag{38}$$

$$\begin{aligned}\frac{\partial\eta}{\partial\tau'}-\vec{U}\cdot(\nabla\eta)=&\frac{1}{RePr}\nabla^2\eta-\frac{Gr}{Re^2}\vec{\xi}\cdot\vec{e}_g\\&+(T-T_m)\sum_{i=1}^{M}\delta(\vec{r}-\vec{r}_i)\end{aligned} \tag{39}$$

Through the aforementioned transformation, the adjoint problem becomes an initial value problem in time τ', and the relevant initial conditions are

$$\xi(X,Y,\tau'=0)=0\quad\text{and}\quad \eta(X,Y,\tau'=0)=0,(X,Y)\epsilon\Omega \tag{40}$$

Finally, only one term would remain when Eqs. (30), (38), and (39) were balanced,

$$D_{\delta Q_u}E(Q_u)=\int_0^{\tau_f}\int_{\Gamma_{uq}}\eta\delta Q_u\,dA\,d\tau=\langle\eta|\delta Q_u\rangle \tag{41}$$

Observing from Eqs. (27) and (41), the gradient of the objective function is equal to the adjoint temperature at the surface where the unknown heat flux is being sought, that is,

$$\nabla E=\eta \tag{42}$$

That holds true in general for an arbitrary heat flux $Q_u(\Gamma_{uq},\tau)$. Additionally, the only driving force of the adjoint problem is the deviation (error) of the predicted temperature T from the desired or measured temperature T_m. As a result, if the objective heat flux were achieved, the T would equal to T_m at the sensor locations.

4. Numerical methodology and implementation

4.1. Implementation of the direct convection problem

Since the flow governed by Eqs. (1)–(3) together with the initial and boundary conditions (6)–(12) is known to be parabolic in time but elliptic in space, the solution for the problem can only be marched in time, and iterative procedures must be employed to obtain the solution in the spatial domain.

Finite volume method (FVM) is applied to discretize the governing equations on a staggered grid system [36]. In the course of discretization, the third-order deferred correction QUICK scheme and second-order central difference scheme are, respectively, are implemented for the convection and diffusion terms [37,38]. The SIMPLE algorithm was chosen to numerically solve the governing differential equations in their primitive form [36]. To obtain better convergence properties, the unsteady terms in these equations were implicitly treated and hence approximated by backward differencing. For each time step, the discretized equations were solved by a line-by-line procedure, combining the tri-diagonal matrix algorithm (TDMA) and the successive over relaxation (SOR) iteration.

The time interval, first set at a relatively small value from 10^{-4} to 10^{-3} depending on *Re*, *Gr*, and Pr is successively enlarged. During the program tests, a systematic grid independence study was conducted, and then the final uniform grid resolution of 51×51 was selected at the balance between the calculation accuracy and the speed for fluid flow in a square vented enclosure.

The convergence criteria are based on maximum errors in global mass and energy imbalances. Convergence was ensured when the maximum errors become less than 10^{-4}. The current numerical technique has been very successfully used and validated in a series of recent papers, including transient conjugate heat transfer [38], conjugate natural convection [21,31,38], double diffusive natural convection in gaseous and porous enclosures [31–34], double diffusive mixed convection [19], and turbulent forced convection in slot-ventilated rooms [39,40]. To further validate the present numerical code, mixed convection in a slot-ventilated enclosure has been numerically analyzed. One of the initial numerical studies on mixed convection in this enclosure was performed by Papanicolaou and Jaluria [8], and Hsu and Wang [13]. For this comparison, solutions presented in Table 1 are obtained for $Re = 100$, $Gr/Re^2 = 1$, $Pr = 0.7$. Observing from Table 1, the agreement between the present study and other published results is fairly good, and the maximum deviation is no more than 3%.

4.2. Implementation of the sensitivity and adjoint problems

Since the sensitivity flow governed by Eqs. (18)–(20) together with the initial and boundary conditions (21)–(26) and the adjoint flow governed by Eqs. (30), (38), and (39) together with the conditions (33)–(36) and the initial condition Eq. (40) are similar to the direct flow, the same convective and diffusive difference schemes used in the implementation of the direct problem are also used in the implementation of the sensitivity and adjoint problems. Additionally, the SIMPLE algorithm is also adopted provided that the set of sensitivity and adjoint equations and boundary conditions were solved sequentially.

Due to the temperature and velocity solutions of the direct problem appear in the sensitivity and adjoint problems, the whole history of the solution for direct problem should be stored for transient situation. It is convenient to carry out the finite volume solution of the sensitivity and adjoint problems with same mesh and time steps as those used to solve the direct problem.

Table 1
Comparison of benchmark solutions in slot-ventilated enclosures.

	[8]	[13]	Present work
Nu	3.0725	3.1134	3.1105
T_{max}	0.3623	0.3473	0.3528
Ψ_{max}	1.3771	1.3676	1.3700

4.3. Conjugate gradient method

After having obtained an analytical expression for the exact gradient of the cost functional, any of the standard functional minimization techniques can be used for solving the above defined optimization problem. The gradient of E as was calculated in Section 3.2 is used in conjunction with the conjugate gradient method [24–28].

As mentioned above, the conjugate search direction ps and the step size α should be defined and calculated. The optimal step size α^K is obtained by minimizing the cost functional E with respect to the scalar α^K, and it has the following formulation:

$$\alpha^K = -\frac{\int_0^{\tau_f} \sum_{i=1}^{M} [T(X_i, Y_i, \tau) - T_m(X_i, Y_i, \tau)] \delta T(X_i, Y_i, \tau) d\tau}{\int_0^{\tau_f} \sum_{i=1}^{M} [\delta T(X_i, Y_i, \tau)]^2 d\tau} \tag{43}$$

where, δT is determined by the convergent sensitivity field. The conjugate search direction ps should require the gradient of cost functional given by Eq. (42), and it can be obtained as follows:

$$ps^K = \begin{cases} -\nabla E^K, & K = 0 \\ -\nabla E^K + \frac{\langle \nabla E^K - \nabla E^{K-1} | \nabla E^K \rangle}{\|\nabla E^{K-1}\|^2} \times ps^{K-1}, & K \geqslant 1 \end{cases} \tag{44}$$

The summary of CGM optimization procedure is presented in Fig. 2, and it is used to minimize the cost functional of Eq. (16). The present algorithm is driven by the thermal solution, i.e., the fields of T, δT, and η; simultaneously, these thermal fields are dynamically calculated with the corresponding flow fields of $\boldsymbol{U}$, $\delta \boldsymbol{U}$, and ξ as illustrated in aforementioned sections.

Since the adjoint temperature field is zero at the final time τ_f, the conjugate direction also vanishes and the estimated value of the heat flux at τ_f is always equal to the initial guess value. Although the conjugate gradient method can be modified to alleviate this difficulty [25], it is not the main purpose of this study to examine the inverse solution at τ_f. The discussion will be restricted to heat fluxes that are zero at τ_f and focus on the effects of convection on the convergence of the algorithm.

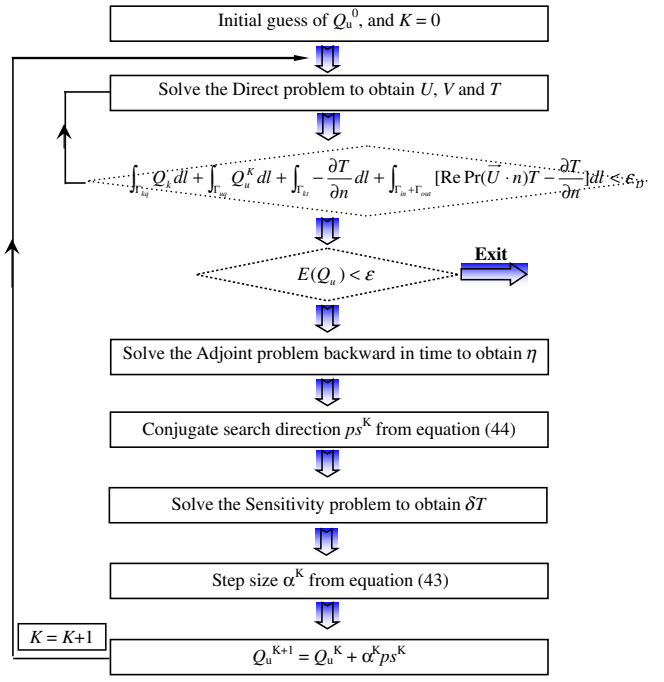

Fig. 2. The conjugate gradient method for inverse mixed convection problem. The convergent criterion ε_D depends on the specific situations.

4.4. Discrepancy principle for stopping criteria

Actually, temperature data recording from the sensors always contain errors. A dimensionless random noise level σ ($\sigma = \sigma^*/\Delta t$) was added to the simulated exact temperature data (average one in practice) to generate the measured temperature data, that is,

$$T_m = T_{exact} + \omega\sigma \tag{45}$$

where σ is the standard deviation of the measurement errors which is assumed to be the same for all measurements, and ω is the Gaussian distributed random number. The value of ω is chosen over the range of $-2.576 \leqslant \omega \leqslant +2.576$, which represents the 99% confidence bound for the temperature measurement. In the present calculation, the noise level σ takes values of 0.00, 0.005, 0.01, and 0.05, which correspond to zero, 1.25%, 2.5%, and 12.5% relative measurement errors, respectively.

If the problem involves no measurement errors, the following traditional condition can be used:

$$E(Q_u^K) < \varepsilon \tag{46}$$

where ε is a small specified number, and can be used as the stopping criterion. However, the observed temperature information contains measurement errors. As a result, the inverse solution will tend to approach the perturbed input data, and the solution will exhibit oscillatory behavior as the number of iterations is increased [22,23]. Numerical experiments have shown that it is advisable to use the discrepancy principle for terminating the iteration process in the regular method. Assuming $T^K - T_m = \sigma$, the discrepancy principle that establishes the value of the stopping criteria ε can be obtained from Eq. (16). For steady situation, it can be written as

$$E(Q_u^K) < \varepsilon^2 = \frac{1}{2}\sum_{i=1}^{M}\sigma^2 \tag{47}$$

If the function E has a minimum value that is larger than ε^2, the following criterion is used to stop the iteration [25,29]:

$$E(Q_u^{K+1}) - E(Q_u^K) < \varepsilon_1 \tag{48}$$

where ε_1 is a prescribed small number depending on the specific situations.

5. Results and discussion

The enclosure considered here is shown in Fig. 1(b), with aspect ratio $H/L = 1.0$ and with two ventilation ports of dimensionless height 0.1. The fluid is air with a Prandtl number $Pr = 0.72$. The entrance ventilation port is kept at the top of the left vertical wall, while the exit port on the bottom of the same side. At the inflow opening, uniform flow conditions are assumed, i.e., $U_{in} = 1.0$ and

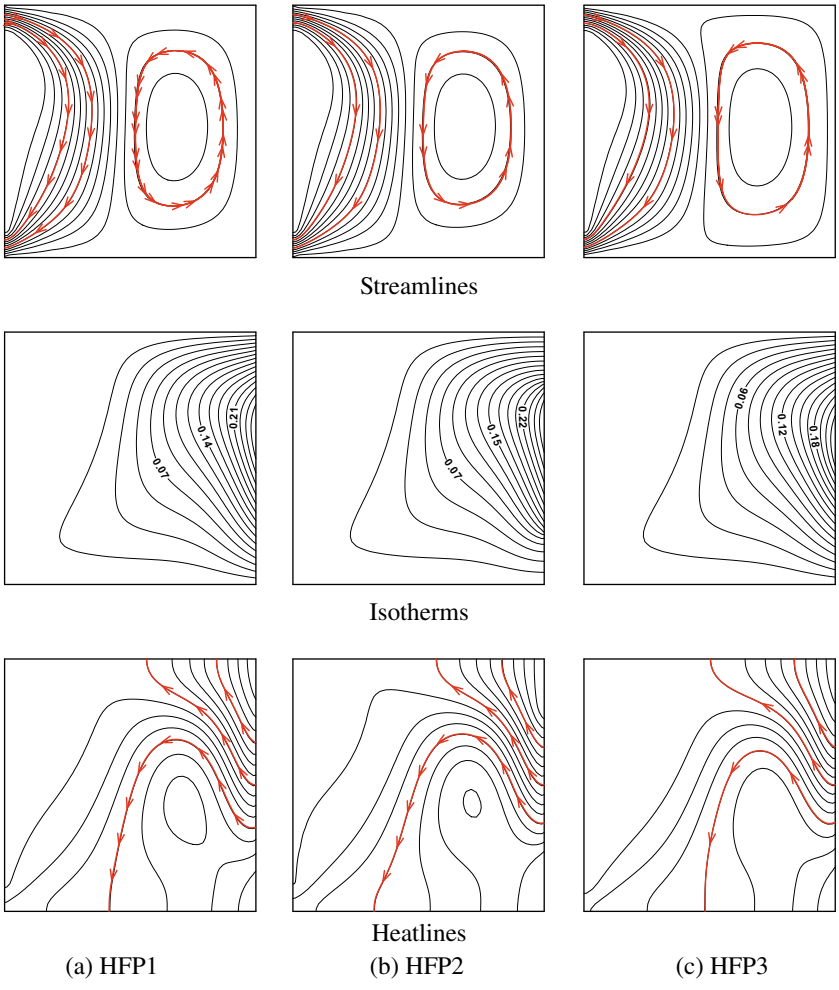

Fig. 3. Calculated contours of streamfunctions (top), isotherms (middle) and heatfunctions (bottom) for $Re = 100$ and $Ri = 2.00$, (a) HFP1, $\Psi_{max} = 0.030$, $\Psi_{min} = -0.097$, $\Theta_{max} = 0.229$, $\Theta_{min} = -0.407$, $T_{max} = 0.278$; (b) HFP2, $\Psi_{max} = 0.030$, $\Psi_{min} = -0.097$, $\Theta_{max} = 0.206$, $\Theta_{min} = -0.393$, $T_{max} = 0.291$; (c) HFP3, $\Psi_{max} = 0.023$, $\Psi_{min} = -0.097$, $\Theta_{max} = 0.192$, $\Theta_{min} = -0.307$, $T_{max} = 0.239$.

$T_{in} = 0.0$; For the boundary condition at the outflow, all the gradients in the horizontal direction are taken as zero, to represent developed flow and thermal fields. The left vertical wall of the square enclosure is adiabatic, $Q_k = 0$. The top and bottom walls both are maintained at constant and uniform temperature $T_k = 0$ and the right wall is imposed by the spatially varying heat flux $Q_u(Y)$ [38,41,42], thus giving rise to free convective fluid flows in the enclosure. Simultaneously, the internal free convection would be interacted with the external flow.

The direct mix convection is investigated firstly. Streamlines and heatlines will be adopted to visualize the fluid flow and heat transport. Effect of heat flux profiles on the flow structure and heat transfer performance is presented and analyzed. Variation Grashof and Reynolds numbers obtains different flow patterns covering forced convection, mixed convection and natural convection. The transition process between forced dominant convection to natural dominant convection has been represented by a critical diagram of the form in terms of Reynolds number and Grashof number.

Inverse mixed convection problem in the present work is to determine the unknown heat flux $Q_u(Y)$ on the right wall, from temperature measurements T_m taken at the sensor's position. When the steady mixed convection state is achieved, the temperature measurements taken at the sensor's locations are conducted. The aforementioned Conjugate Gradient Method will be adopted to solve the inverse mixed convection problem.

Inverse solutions are firstly obtained from exact simulated data ($\sigma = 0$). The effects of Richardson number *Ri*, Reynolds number *Re*, type of boundary heat flux on the inverse mixed convection solutions would be discussed in the following sections. Effects of random errors on the inverse solutions would be considered subsequently. In this work, all CGM computations start from $Q_u^0 = 0$ as initial guess for the heat flux. Additionally, the sensors are assumed to be uniformly placed by a layer of 50 thermocouples at ($X_m = 0.90$, $0.00 \leqslant Y_m \leqslant 1.00$), where is adjacent to the unknown boundary conditions.

5.1. Direct mixed convection and its visualization

As illustrated in these figures, the streamfunction is used to identify the sense and magnitude of the fluid circulation. The coordinates are chosen such that counterclockwise (or clockwise) movement will be associated with positive (or negative) Ψ. Similar relations are set for heat flow and heatfunction Θ [19,30–35]. The intervals of these computed streamlines, isotherms and heatlines are $\Delta\varphi = (\varphi_{max} - \varphi_{min})/16$, where φ stands for Ψ, T or Θ. Because it is not possible to include the results for all boundary conditions at all Reynolds and Richardson numbers due to space limitation, some representative streamlines, isotherms and heatlines are shown for various boundary heat flux, *Re* and *Ri* in Figs. 3–6.

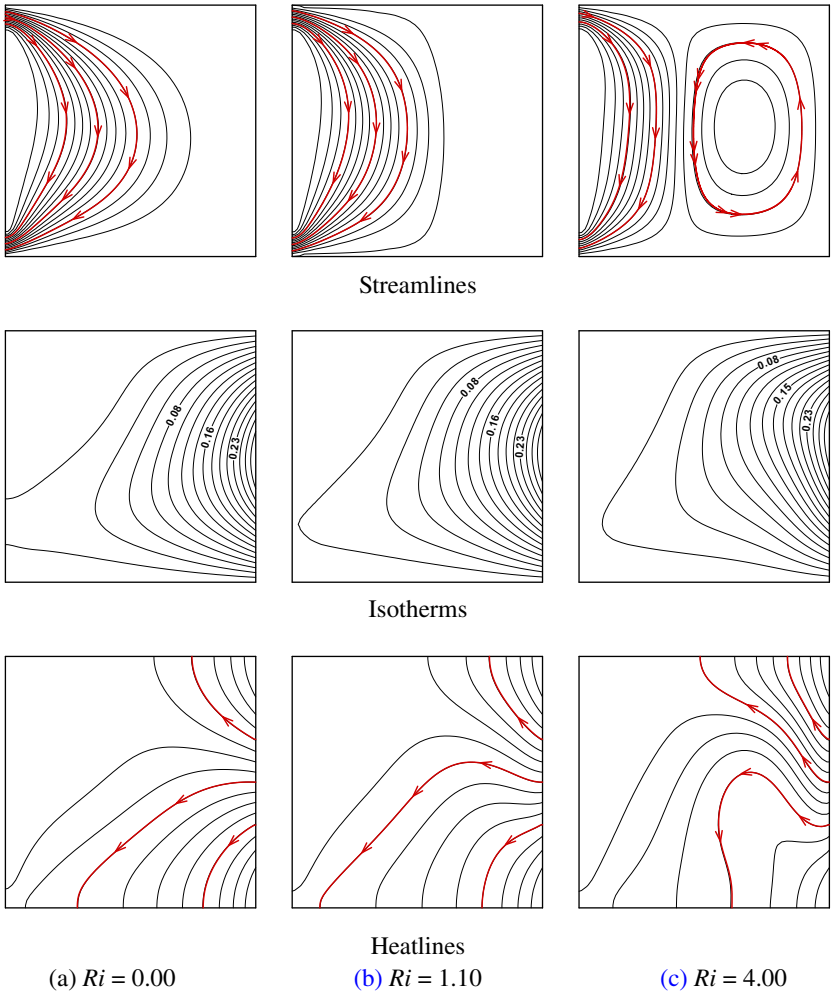

Fig. 4. Calculated contours of streamfunctions (top), isotherms (middle) and heatfunctions (bottom) for *Re* = 50 and HFP1, and (a) *Ri* = 0.00, $\Psi_{max} = 0.000$, $\Psi_{min} = -0.095$, $\Theta_{max} = 0.376$, $\Theta_{min} = -0.260$; (b) *Ri* = 1.10, $\Psi_{max} = 0.006$, $\Psi_{min} = -0.095$, $\Theta_{max} = 0.341$, $\Theta_{min} = -0.294$; (c) *Ri* = 4.00, $\Psi_{max} = 0.036$, $\Psi_{min} = -0.095$, $\Theta_{max} = 0.264$, $\Theta_{min} = -0.372$.

5.1.1. Effect of heat flux profiles on direct mixed convection

The following well-defined functions of heat flux Q_u have been, respectively, employed along the right wall:

$$Q_u(Y) = -\sin(\pi Y),\ 0 \leqslant Y \leqslant 1 \text{ (HFP1, semi-cycle sinusoidal function)} \quad (49a)$$

$$Q_u(Y) = \begin{cases} -1, & 0.2 \leqslant Y \leqslant 0.8 \\ 0, & Y \in [0,0.2] \cup [0.8,1.0] \end{cases} \text{ (HFP2, step function)} \quad (49b)$$

$$Q_u(Y) = \begin{cases} -2Y, & 0 \leqslant Y \leqslant 0.5 \\ 2Y-2, & 0.5 \leqslant Y \leqslant 1.0 \end{cases} \text{ (HFP3, triangular function)} \quad (49c)$$

when *Re* and *Ri* maintain at 100 and 2.00, respectively, the fluid and heat transport structures are plotted in Fig. 3 as functions of heat flux profiles. A similar flow structure, the cold external flow squeezing by the counter-clockwise flow eddy, is observed under the heat flux conditions of HFP1, HFP2, and HFP3. Also, the heat transport structures illuminated by the heatlines tend to be similar. The value of Ψ_{max} measuring the flow intensity of the counter-clockwise eddy achieves the minimum as the HFP3 imposes. This is due to the fact that their total heat flow rates ($|\int_0^1 Q_{uX=1} dY|$) decrease (0.636, 0.6, and 0.5 for HFP1, HFP2, and HFP3, respectively). Simultaneously, the maximum temperature across the system T_{max} attains minimum as the HFP3 imposes. Here should be noted that, the value of T_{max} under HFP2 situation exceeds that of HFP1, which results from the fact that the heat flux distributes more concentrated in the former case.

5.1.2. Effect of Grashof and Reynolds numbers on direct mixed convection

Due to the little differences between the flow patterns observed in Fig. 3, only the HFP1 is imposed on the right wall. The values chosen for the Reynolds number were in the range of 50–500, these being in the laminar regime. At each of these values of *Re*, the variation of Grashof number expressed in terms of the Richardson number *Ri* was varied from 0 to 6.0, encompassing a range of dominating forced convection to dominating natural convection.

Analysis of complex mixed convection flow physics in the enclosure is difficult due to the interaction between the forced and natural convection. Intuitive inferences are sometimes contrary to the reality. Nevertheless, the air flow and heat transport structures for all the simulations were closely scrutinized, typically presenting in Figs. 4–6. At any *Re*, for *Ri* approaching zero, forced convection dominates and the major flow is clockwisely rotating from the inlet to the outlet. The recirculation zones expand towards the right wall with increasing Reynolds number. Particularly, diffusive thermal transport shown in Fig. 4(a) has been passively strengthened, resulting the heat directly flows toward the outlet, typically shown by the heatlines in Figs. 5 and 6 (a). Correspondingly, there are large thermal gradients adjacent to the heat source.

For higher Gr/Re^2, the buoyancy effects are much stronger and lead to large recirculating cells, while the region that is affected by the source becomes smaller. Such as *Ri* = 4.0, presented in Figs.

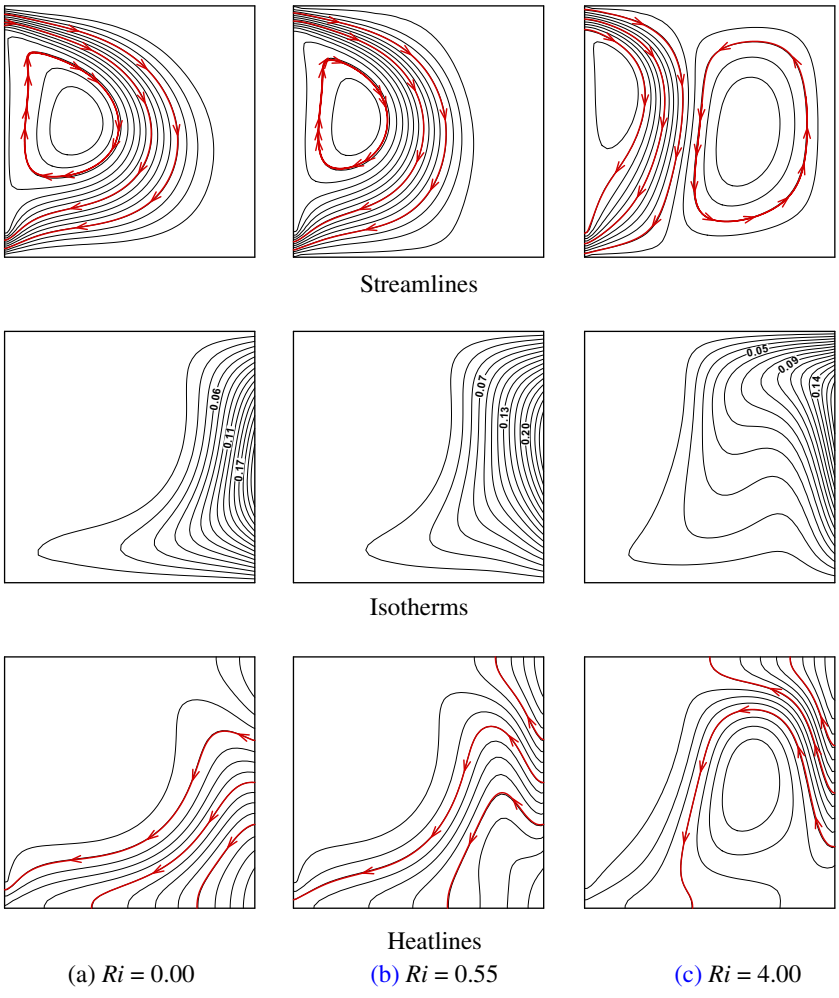

Fig. 5. Calculated contours of streamfunctions (top), isotherms (middle) and heatfunctions (bottom) for *Re* = 200 and HFP1, and (a) *Ri* = 0.00, Ψ_{max} = 0.001, Ψ_{min} = −0.128, Θ_{max} = 0.395, Θ_{min} = −0.241; (b) *Ri* = 0.55, Ψ_{max} = 0.007, Ψ_{min} = −0.123, Θ_{max} = 0.297, Θ_{min} = −0.339; (c) *Ri* = 4.00, Ψ_{max} = 0.047, Ψ_{min} = −0.107, Θ_{max} = 0.257, Θ_{min} = −0.470.

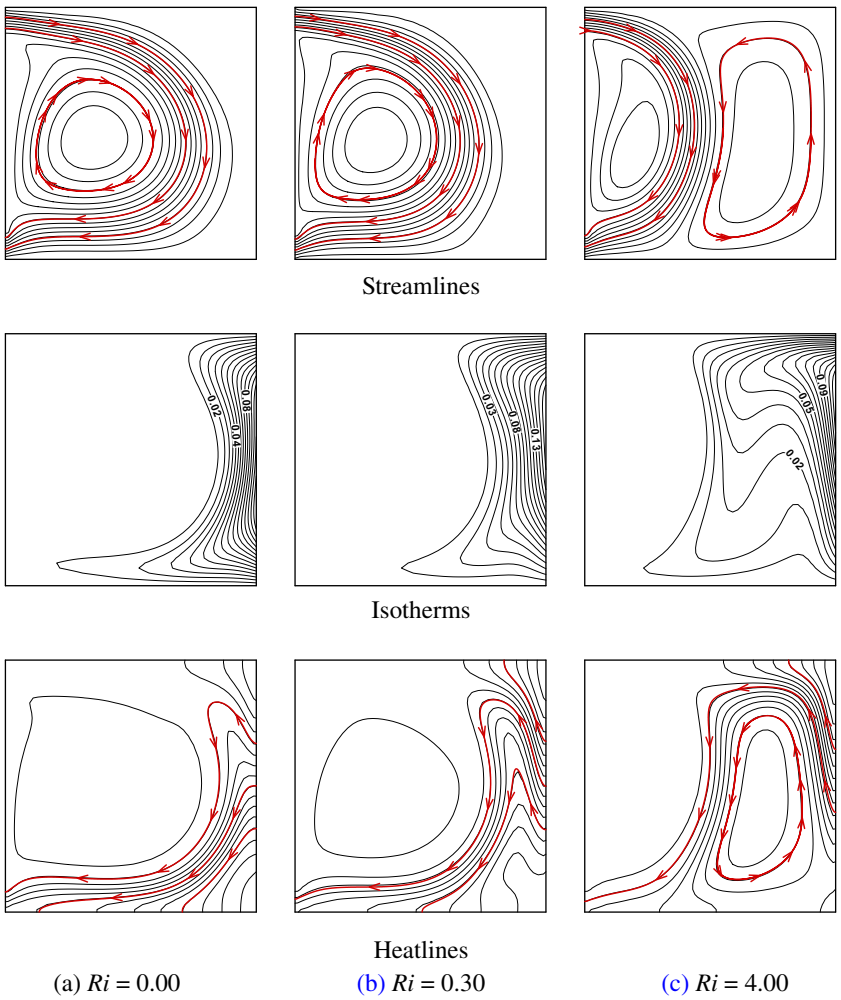

Fig. 6. Calculated contours of streamfunctions (top), isotherms (middle) and heatfunctions (bottom) for $Re = 500$ and HFP1, and (a) $Ri = 0.00$, $\Psi_{max} = 0.001$, $\Psi_{min} = -0.128$, $\Theta_{max} = 0.395$, $\Theta_{min} = -0.241$; (b) $Ri = 0.30$, $\Psi_{max} = 0.007$, $\Psi_{min} = -0.123$, $\Theta_{max} = 0.297$, $\Theta_{min} = -0.339$; (c) $Ri = 4.00$, $\Psi_{max} = 0.047$, $\Psi_{min} = -0.107$, $\Theta_{max} = 0.257$, $\Theta_{min} = -0.470$.

4–6(c), the right counter-clockwise rotating cell squeezes the left clockwise rotating cross flow. Additionally, the formation of thermal plume also becomes evident as *Ri* increases. The development of two distinct regions with large temperature gradients has also been noticed. One of these seems to surround the heat source, while the other one, at a lower temperature level, appears as stratified and horizontal layer of air, almost occupying right half enclosure. These regions become thinner when *Ri* is increased, as expected from a greater upward buoyancy force. It is also noted that the cold external flow does not simply pass through the enclosure, its movement rightward toward the source increases with the Reynolds number. This effect is to enhance the recirculation due to buoyancy by a shearing force while getting heated as it flows though the enclosure. The heat is thus transferred from the recirculating flow to the external flow stream by diffusion. This is also demonstrated by the recirculating heatline structures [31].

For intermittent Gr/Re^2, the buoyancy effect and the forced flow effect could be comparable, the interaction between external cold flow and internal thermal plume could results in the weak interface shear force, and the heat transfer rate unexpectedly decreases with increasing *Ri*, as presented in Fig. 7(a). Simultaneously, the heat dissipation of this system could be impaired, observing from fact that the T_{max} peaks as *Ri* equals to 1.10, 0.65, 0.55, 0.50, and 0.30, respectively, when Reynolds number is maintained at 50, 100, 200, 300, and 500. When thermal plume increases in strength and size, i.e., *Ri* exceeds the critical point (discussing later), the heat transfer rate could be promoted again, where natural convection heat transfer is dominated.

Actually, the relations between the natural convection and forced convection could be determined. Aforementioned convective mass and heat transport structures, typically shown in Figs. 4–6(b), illuminate that the maximal competition between the internal natural convection and external forced convection could result in minimal heat transfer rates. The effect of the Reynolds and Grashof numbers on the convective heat transfer then could be represented by a critical diagram of the form shown in Fig. 8, where the corresponding heat transfer rate attains the lowest value. The general linear fitting correlation of the form is expressed as

$$Re = 5.346 + 0.0056\,Gr \tag{50}$$

As expected, the critical Grashof number increases with the Reynolds number. Physically, internal natural convection invigorates in order to accommodate with the strengthened external forced convection. Particularly, the transition from the forced convection dominated flow to the natural convection dominated flow is clearly seen in Fig. 8, and the former regime beyond the straight line, while the latter regime below it.

5.2. Inverse mixed convection and its visualization

In the case of the inverse mixed convection problem, the wall heat flux Q_u will be predicted from knowledge of the $M = 50$

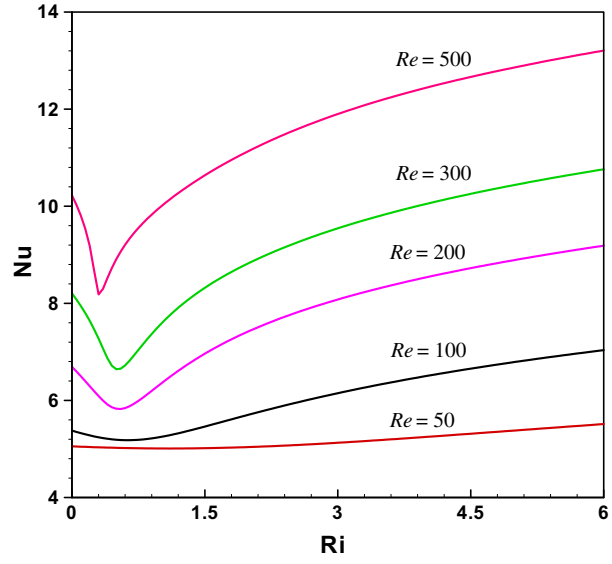

(a) *Nu-Ri*

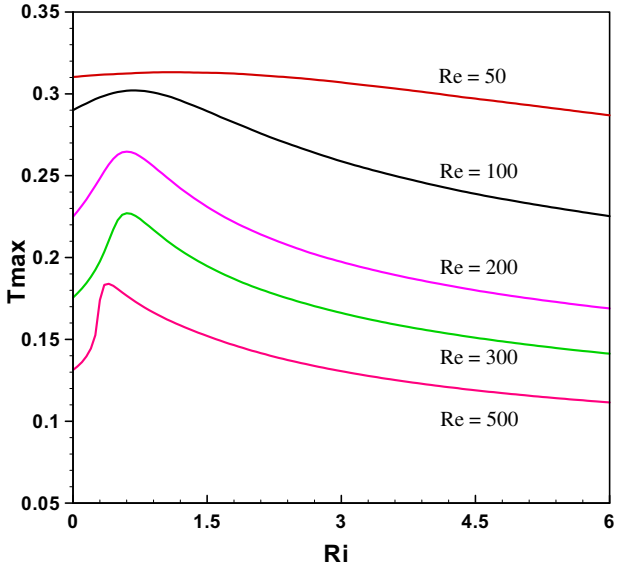

(b) T_{max}-*Ri*

Fig. 7. The average Nusselt number *Nu* and maximum temperature T_{max} as functions of the Richardson number with the Reynolds number as a parameter.

temperature measurements taken along the vertical line $X_m = 0.90$, $0.00 \leqslant Y_m \leqslant 1.00$. In other words, the T_m ($X_m = 0.9$, $0 \leqslant Y_m \leqslant 1$) obtained from the aforementioned direct simulation is simulated as the measurements. The direct, sensitivity, and adjoint problems described earlier are solved and combined with CGM. The stop criterion is set equal to 10^{-6}. The efficiency and accuracy of the present inverse analysis for estimating the spatially varying function of an unknown wall heat flux Q_u at the right wall can be examined from the following figures. The accuracy of the estimation is quantified by the following definition of estimation error:

$$FED = \frac{\|Q_u - Q_{exact}\|^2}{\|Q_{exact}\|^2} \tag{51}$$

5.2.1. Effect of mixed convection states

Observing from Figs. 9–11, the unknown heat flux profiles have been recovered well under different flow states. However, after

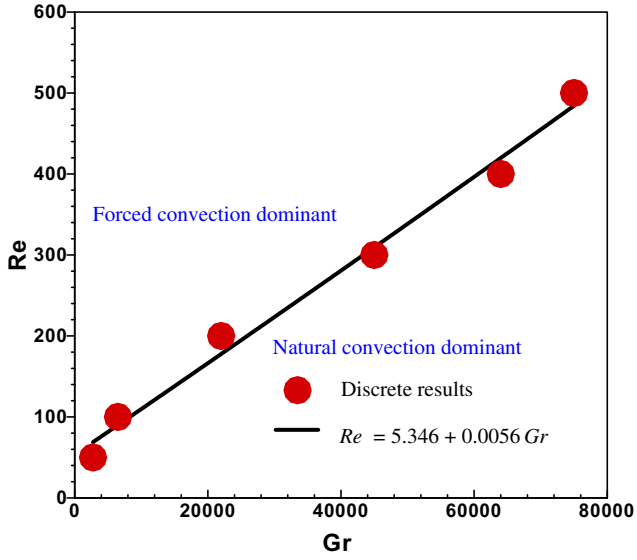

Fig. 8. Critical analysis of the mixed convection flow in the cavity in terms of minimal heat transfer rates for the transition from forced convection dominant flow to natural convection dominant flow.

clearly securitization and comparison, the accuracy of estimation is generally decreased with increasing Reynolds number, either forced convection ($Ri = 0$) or natural convection dominated flow ($Ri = 4$). Boundary heat flux can be recovered with less iterations of CGM when the Reynolds number is no more than 200. However, more CGM iterations are required to obtain the correct profile and amplitude as *Re* increases up to 500. Observing from the heatline transport structures illuminated in Fig. 4–6, more heat has been transported to the outlet with increasing Reynolds number, which has weakened the temperature sensitivities where the temperature sensors are located.

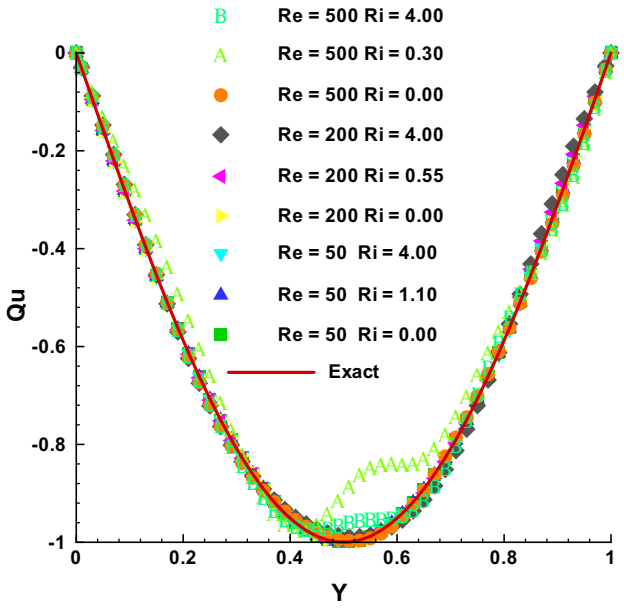

Fig. 9. Effect of Reynolds and Richardson numbers on the inverse mixed convection solution for HFP1, and $\sigma = 0$. (■) $Re = 50$, $Ri = 0.00$, FED = 1.23 _ 10_6, $K = 3$; (▲) $Re = 50$, $Ri = 1.10$, FED = 2.61×10^{-6}, $K = 4$; (▼) $Re = 50$, $Ri = 4.00$, FED = 1.86×10^{-5}, $K = 5$; (▶) $Re = 200$, $Ri = 0.00$, FED = 4.64×10^{-5}, $K = 5$; (◀) $Re = 200$, $Ri = 0.55$, FED = 6.59×10^{-5}, $K = 12$; (◆) $Re = 200$, $Ri = 4.00$, FED = 4.32×10^{-4}, $K = 8$; (●) $Re = 500$, $Ri = 0.00$, FED = 1.02×10^{-4}, $K = 8$; (A) $Re = 500$, $Ri = 0.30$, FED = 7.04×10^{-3}, $K = 98$; (B) $Re = 500$, $Ri = 4.00$, FED = 6.38×10^{-4}, $K = 12$.

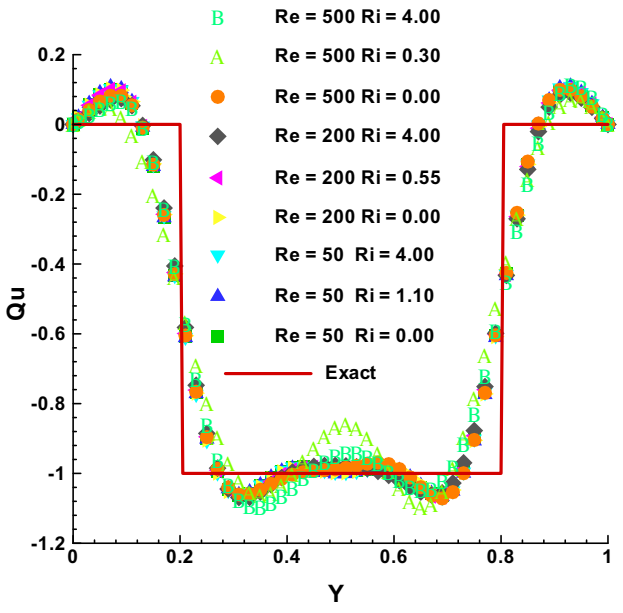

Fig. 10. Effect of Reynolds and Richardson numbers on the inverse mixed convection solution for HFP2, and $\sigma = 0$. ( ) $Re = 50$, $Ri = 0.00$, FED $= 3.56 \times 10^{-2}$, $K = 86$; ( ) $Re = 50$, $Ri = 1.10$, FED $= 3.57 \times 10^{-2}$, $K = 64$; ( ) $Re = 50$, $Ri = 4.00$, FED $= 3.55 \times 10^{-2}$, $K = 53$; ( ) $Re = 200$, $Ri = 0.00$, FED $= 3.50 \times 10^{-2}$, $K = 78$; ( ) $Re = 200$, $Ri = 0.55$, FED $= 3.61 \times 10^{-2}$, $K = 100$; ( ) $Re = 200$, $Ri = 4.00$, FED $= 3.58 \times 10^{-2}$, $K = 46$; ( ) $Re = 500$, $Ri = 0.00$, FED $= 3.49 \times 10^{-2}$, $K = 29$; (A) $Re = 500$, $Ri = 0.30$, FED $= 4.93 \times 10^{-2}$, $K = 36$; (B) $Re = 500$, $Ri = 4.00$, FED $= 4.10 \times 10^{-2}$, $K = 32$.

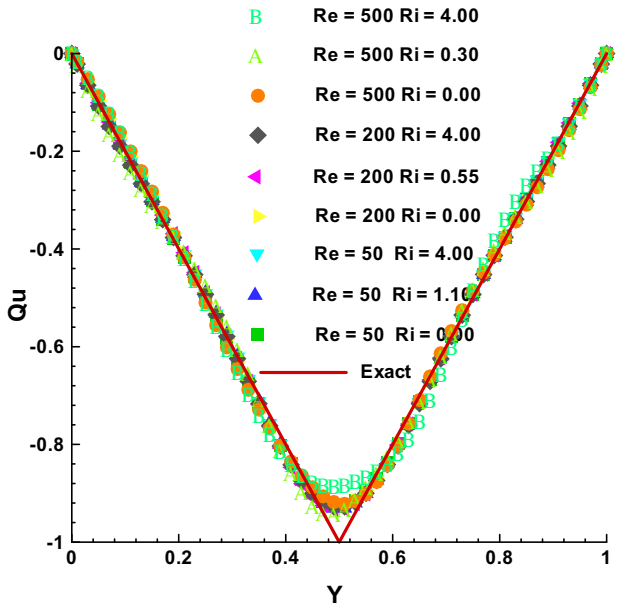

Fig. 11. Effect of Reynolds and Richardson numbers on the inverse mixed convection solution for HFP3, and $\sigma = 0$. ( ) $Re = 50$, $Ri = 0.00$, FED $= 6.47 \times 10^{-4}$, $K = 16$; ( ) $Re = 50$, $Ri = 1.10$, FED $= 5.58 \times 10^{-4}$, $K = 15$; ( ) $Re = 50$, $Ri = 4.00$, FED $= 6.03 \times 10^{-4}$, $K = 22$; ( ) $Re = 200$, $Ri = 0.00$, FED $= 7.86 \times 10^{-4}$, $K = 10$; ( ) $Re = 200$, $Ri = 0.55$, FED $= 6.39 \times 10^{-4}$, $K = 16$; ( ) $Re = 200$, $Ri = 4.00$, FED $= 7.00 \times 10^{-4}$, $K = 13$; ( ) $Re = 500$, $Ri = 0.00$, FED $= 1.18 \times 10^{-3}$, $K = 9$; (A) $Re = 500$, $Ri = 0.30$, FED $= 1.17 \times 10^{-3}$, $K = 20$; (B) $Re = 500$, $Ri = 4.00$, FED $= 3.34 \times 10^{-3}$, $K = 11$.

Differing from the monotonic functions between FED and Reynolds number, the accuracy of inverse convection calculation almost varies little with Richardson numbers. Actually, the strength of internal natural convection hardly changes the thermal boundary layer structures adjacent to the right wall; overall estimation of boundary heat fluxes is thus less affected by the variation of Richardson number. Additionally, FED values were achieved a bit higher in transitional flow regime for most of the studied cases (Grashof number and Reynolds number satisfying Eq. (50)), where a certain loss of accuracy exists as interaction between forced convection and free convection builds up and reduces the sensitivity of the algorithm.

5.2.2. Effect of unknown heat flux profiles

These heat flux profiles imposed on the active boundary, namely, the step, triangular and sinusoidal functions have been respectively depicted in Figs. 9–11. Comparing these results with identical governing parameters, the accuracy of the inverse solution for step heat flux is evidently lower than that of other func-

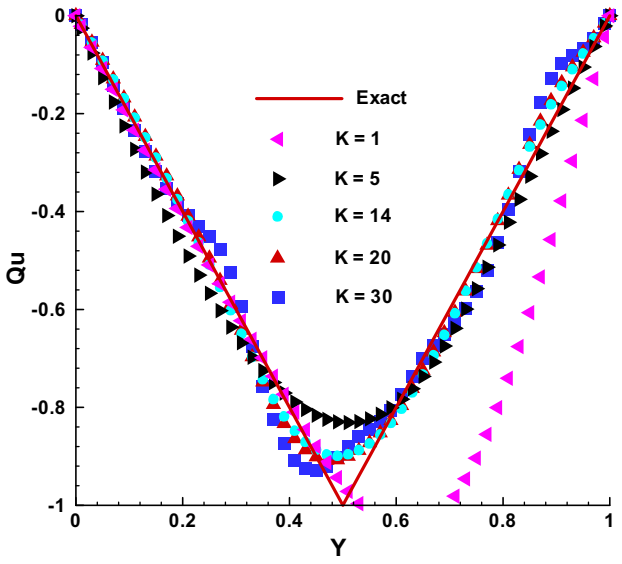

(a) Effect of iteration loops K, $\sigma = 0.01$

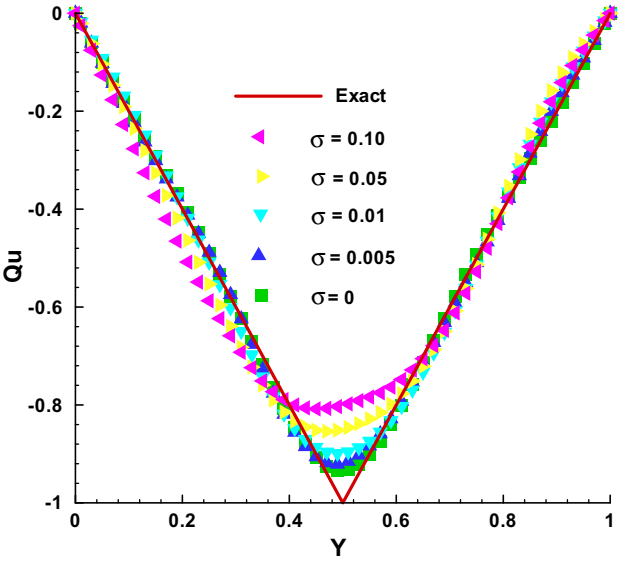

(b) Effect of standard deviation σ

Fig. 12. The effect of noise level σ on the inverse estimating HFP3 with $Re = 200$ and $Ri = 0.55$. (a) Estimated heat flux as a function of CGM iterations with constant level $\sigma = 0.01$; (b) estimated heat flux as a function of standard deviation, and (b1) $\sigma = 0.00$, FED $= 6.39 \times 10^{-4}$, $K = 16$; (b2) $\sigma = 0.005$, FED $= 1.14 \times 10^{-3}$, $K = 27$; (b3) $\sigma = 0.01$, FED $= 2.58 \times 10^{-3}$, $K = 14$; (b4) $\sigma = 0.05$, FED $= 7.18 \times 10^{-3}$, $K = 6$; (b5) $\sigma = 0.10$, FED $= 1.40 \times 10^{-2}$, $K = 4$.

tions. Essentially, the step flux (HFP2) with Fourier coefficients inversely proportional to n could be recovered more difficult than the triangular flux (HFP3), with Fourier coefficients inversely proportional to n^2. Furthermore, these fluxes with a spectrum involving many frequency components, such as step function and triangular function, can be reproduced more difficult than those of single frequency such sinusoidal functions (HFP1). As a result, the accuracy of the inverse solution illuminated in Fig. 9 is generally achieved higher, with less CGM iterations, than those presented in Figs. 10 and 11.

5.2.3. Effect of measurement errors

In practical experimental situations, it is expected that some errors will be introduced into the measurements. The simulated measurements containing random measurement errors have been generated from Eq. (45). When inverse mixed convection problems are solved using these noisy data, the iterative regularization effect of the conjugate gradient on the solution can be detected just as well as in conduction, and used with much profit to optimize the final result [23]. That has been demonstrated evidently in Fig. 12(a), where a reasonably accurate solution could be obtained after 14 CGM iterations for estimating HFP3 with $\sigma = 0.01$. The solution obtained after 20 and 30 CGM iterations separately, when the high frequency components of the noises embedded in the data are recovered, appears far less satisfactory in comparison. This feature allows the satisfactory prediction of an unknown heat flux from noisy temperature data, by stopping the iteration process before the undesirable components of the noise are recovered.

It is observed from Fig. 12(b) that the convergence of the solution strongly depends on the frequency of the T_m data. The convergence speed of the inverse solution slows down as frequency increases. Some bias remains in the solution, and it could be reduced by taking the sensors closer to active boundary, but at the expense of a greater sensitivity to the higher noise frequency components [28]. Fig. 12(b) reveals that the accuracy of estimation deteriorates as the noise level increases, but the results are still good in all these situations.

6. Conclusions

Direct and inverse mixed convection problems have been investigated together in the present work. The finite-volume method and pressure-based SIMPLE algorithm are adopted to solve the direct, sensitivity and adjoint problems by enforcing global mass conservations. Estimation of boundary heat fluxes is conducted by employing the Fletcher–Reeves conjugate gradient method.

The fluid and heat transports, affected by the Reynolds number, Richardson number and functional forms of boundary heat fluxes, have been vividly analyzed by streamlines and heatlines, respectively. Visualization results thus provide vigorous means to discuss the interaction between external forced convection and internal natural convection. Flow and heat transport structures are less affected by the heat flux profiles. Flow states of mixed convection, including forced convection dominated, transitional flow, and natural convection dominated, are delineated by Reynolds and Richardson numbers, the critical correlations are produced in terms of minimum heat transfer rates, where the heat dissipation of this system could be impaired greatly.

Concerning the inverse mixed convection problem, the accuracy of solution and the sensitivity of the algorithm generally reduce with increasing Reynolds number, and tend be affected little by Richardson number, although more CGM iterations are needed for inverse estimation at the transitional flow regime.

Boundary heat fluxes with a spectrum involving many frequency components (step function HFP2 and triangular function HFP3) are reproduced more difficult than those of single frequency (sinusoidal function HFP1). Stable solutions may be obtained from noisy data by stopping the iteration process before the high frequency components of the random noises start to affect significantly the inverse solution. The accuracy of heat flux estimation and the convergence speed of CGM both deteriorate as the standard deviation of temperature measurement increases.

Without any a priori information, the developed algorithm and procedure are capable of predicting an arbitrary heat flux function from temperature measured by sensors located within the cavity. The developed analysis for the calculation of the gradient of the cost functional is general and can be applied to other mixed convection control or re-construction problems. Additionally, other extensions, including inner heat sources and real-time determination of unknown sources, are currently under investigations.

Acknowledgements

The authors wish to express their appreciation for support from the National Natural Science Foundation of China (No. 50578059).

References

[1] B. Gebhart, Y. Jaluria, R.L. Mahajan, B. Sammakia, Buoyancy Induced Flow and Transport, Hemisphere, Washington, DC, 1988.
[2] T. Cebeci, Convective Heat Transfer, Springer, Berlin, 2002.
[3] W.L. Oberkampf, L.I. Crow, Numerical study of the velocity and temperature fields in a flow-through reservoir, ASME J. Heat Transfer 98 (1976) 353–359.
[4] E.M. Sparrow, F. Samie, Interaction between a stream which passes through an enclosure and natural convection within the enclosure, Int. J. Heat Mass Transfer 25 (1982) 1489–1502.
[5] T.S. Lee, Laminar fluid and heat flow through an opened rectangular cooling chamber, Int. J. Heat Fluid Flow 12 (1991) 249–256.
[6] E. Papanicolaou, Y. Jaluria, Mixed convection from an isolated heat source in a rectangular enclosure, Numer. Heat Transfer, Part A 18 (1990) 427–461.
[7] E. Papanicolaou, Y. Jaluria, Transition to a periodic regime in mixed convection in a square cavity, J. Fluid Mech. 239 (1992) 489–509.
[8] E. Papanicolaou, Y. Jaluria, Mixed convection flow from a localized heat source in a cavity with conducting walls: a numerical study, Numer. Heat Transfer, Part A 23 (1993) 463–484.
[9] E. Papanicolaou, Y. Jaluria, Mixed convection from simulated electronic components at varying relative positions in a cavity, ASME J. Heat Transfer 116 (1994) 960–970.
[10] E. Papanicolaou, Y. Jaluria, Computation of turbulent flow in mixed convection in a cavity with a localized heat source, ASME J. Heat Transfer 117 (1995) 649–658.
[11] T.H. Hsu, P.T. Hsu, S.P. How, Mixed convection in a partially divided rectangular enclosure, Numer. Heat Transfer, Part A 31 (1997) 655–683.
[12] V.V. Calmidi, R.L. Mahajan, Mixed convection over a heated horizontal surface in a partial enclosure, Int. J. Heat Fluid Flow 19 (1998) 358–367.
[13] T.H. Hsu, S.G. Wang, Mixed convection in a rectangular enclosure with discrete heat sources, Numer. Heat Transfer, Part A 38 (2000) 627–652.
[14] D. Angirasa, Mixed convection in a vented enclosure with an isothermal vertical surface, Fluid Dyn. Res. 26 (2000) 219–233.
[15] H. van Santen, Chris R. Kleijn, E.A. Harry, On multiple stability of mixed-convection flows in a chemical vapor deposition reactor, Int. J. Heat Mass Transfer 44 (2001) 659–672.
[16] G.C. Buscaglia, E.A. Dari, Numerical investigation of flow through a cavity with internal heat generation, Numer. Heat Transfer, Part A 43 (2003) 525–541.
[17] M.T. Bhoite, G.S.V.L. Narasimham, M.V.K. Murthy, Mixed convection in a shallow enclosure with a series of heat generating components, Int. J. Therm. Sci. 44 (2005) 121–135.
[18] S. Mahmud, I. Pop, Mixed convection in a square vented enclosure filled with a porous medium, Int. J. Heat Mass Transfer 49 (2006) 2190–2206.
[19] W. Chen, F.Y. Zhao, G.F. Tang, D. Liu, Transportation of indoor double diffusive mixed convection coupled with diffusion in solid walls, J. HV&AC 36 (2006) 12–18.
[20] E. Bilgen, A. Muftuoglu, Cooling strategy by mixed convection of a discrete heater at its optimum position in a square cavity with ventilation ports, Int. Commun. Heat Mass Transfer 35 (2008) 545–550.
[21] F.Y. Zhao, G.F. Tang, D. Liu, Conjugate natural convection in enclosures with external and internal heat sources, Int. J. Eng. Sci. 44 (2006) 148–165.
[22] O.M. Alifanov, Inverse Heat Transfer Problems, Springer, Berlin, 1996.
[23] M.N. Ozisik, H.R.B. Orlande, Inverse Heat Transfer: Fundamentals and Applications, Taylor & Francis, New York, 2000.
[24] N. Zabaras, G.Z. Yang, A functional optimization formulation and implementation of an inverse natural convection problem, Comput. Meth. Appl. Mech. Eng. 144 (1997) 245–274.

[25] H.M. Park, O.Y. Chung, Reduction of modes for the solution of inverse natural convection problems, Comput. Meth. Appl. Mech. Eng. 190 (2000) 919–940.
[26] R. Sampath, N. Zabaras, A functional optimization approach to an inverse magneto-convection problem, Comput. Meth. Appl. Mech. Eng. 190 (2001) 2063–2097.
[27] M.J. Colaco, H.R.B. Orlande, Inverse natural convection problem of simultaneous estimation of two boundary heat fluxes in irregular cavities, Int. J. Heat Mass Transfer 47 (2004) 1201–1215.
[28] F.Y. Zhao, D. Liu, G.F. Tang, Numerical determination of boundary heat fluxes in an enclosure dynamically with natural convection through Fletcher–Reeves gradient method, Comput. Fluids 38 (2009) 797–809.
[29] F.Y. Zhao, D. Liu, G.F. Tang, Inverse determination of boundary heat fluxes in a porous enclosure dynamically coupled with thermal transport, Chem. Eng. Sci. 64 (2009) 1390–1403.
[30] V.A.F. Costa, Bejan's heatlines and masslines for convection visualization and analysis, Appl. Mech. Rev. 59 (2006) 126–145.
[31] F.Y. Zhao, D. Liu, G.F. Tang, Application issues of the streamline heatline, and massline for conjugate heat and mass transfer, Int. J. Heat Mass Transfer 50 (2007) 320–334.
[32] F.Y. Zhao, D. Liu, G.F. Tang, Multiple steady flows in confined gaseous double diffusion with discrete thermosolutal sources, Phys. Fluids 19 (2007) 107103.
[33] F.Y. Zhao, D. Liu, G.F. Tang, Natural convection in a porous enclosure with a partial heating and salting element, Int. J. Therm. Sci. 47 (2008) 569–583.
[34] F.Y. Zhao, D. Liu, G.F. Tang, Natural convection in an enclosure with localized heating and salting from below, Int. J. Heat Mass Transfer 51 (2008) 2889–2904.
[35] A. Dalal, M.K. Das, Heatline method for the visualization of natural convection in a complicated cavity, Int. J. Heat Mass Transfer 51 (2008) 263–272.
[36] S.V. Patankar, Numerical Heat Transfer and Fluid Flow, Hemisphere, Washington, DC, 1980.
[37] T. Hayase, J.A.C. Humphrey, R. Greif, A consistently formulated QUICK scheme for fast and stable convergence using finite-volume iterative calculation procedure, J. Comput. Phys. 98 (1992) 108–118.
[38] D. Liu, F.Y. Zhao, G.F. Tang, Conjugate heat transfer in an enclosure with a centered conducting body imposed sinusoidal temperature profiles on one side, Numer. Heat Transfer, Part A 53 (2008) 204–223.
[39] D. Liu, F.Y. Zhao, G.F. Tang, Numerical analysis of two contaminants removal from a three-dimensional cavity, Int. J. Heat Mass Transfer 51 (2008) 378–382.
[40] F.Y. Zhao, D. Liu, G.F. Tang, Multiple steady fluid flows in a slot-ventilated enclosure, Int. J. Heat Fluid Flow 29 (2008) 1295–1308.
[41] E. Bilgen, R.B. Yedder, Natural convection in enclosure with heating and cooling by sinusoidal temperature profiles on one side, Int. J. Heat Mass Transfer 50 (2007) 139–150.
[42] T.T.M. Onyango, D.B. Ingham, D. Lesnic, Reconstruction of boundary condition laws in heat conduction using the boundary element method, Comput. Math. Appl. 57 (2009) 153–168.